wind

Article

Icing Wind Tunnel and Erosion Field Tests of Superhydrophobic Surfaces Caused by Femtosecond Laser Processing

Roland Fürbacher *, Gerhard Liedl, Gabriel Grünsteidl and Andreas Otto

Institute of Production Engineering and Photonic Technologies, TU Wien, Getreidemarkt 9, 1060 Vienna, Austria
* Correspondence: roland.fuerbacher@tuwien.ac.at

Abstract: Ice accumulation on lift-generating surfaces, such as rotor blades or wings, degrades aerodynamic performance and increases various risks. Active measures to counteract surface icing are energy-consuming and should be replaced by passive anti-icing surfaces. Two major categories of surface treatments—coating and structuring—already show promising results in the laboratory, but none fulfill the current industry requirements for performance and durability. In this paper, we show how femtosecond laser structuring of stainless steel (1.4301) combined with a hydrocarbon surface treatment or a vacuum treatment leads to superhydrophobic properties. The anti-ice performance was investigated in an icing wind tunnel under glaze ice conditions. Therefore, flexible steel foils were laser-structured, wettability treated and attached to NACA 0012 air foil sections. In the icing wind tunnel, hydrocarbon treated surfaces showed a 50 s ice build-up delay on the leading edge as well as a smoother ice surface compared to the reference. To demonstrate the erosion resistance of these surfaces, long-term field tests on a small-scale wind turbine were performed under alpine operating conditions. The results showed only minor erosion wear of micro- and nano-structures after a period of six winter months.

Keywords: wind turbine icing; airfoil icing; surface modification; femtosecond laser structuring; superhydrophobic surface; icephobic surface; hydrocarbon treatment; vacuum treatment; erosion resistance

check for updates

Citation: Fürbacher, R.; Liedl, G.; Grünsteidl, G.; Otto, A. Icing Wind Tunnel and Erosion Field Tests of Superhydrophobic Surfaces Caused by Femtosecond Laser Processing. *Wind* **2024**, *4*, 155–171. https://doi.org/10.3390/wind4020008

Academic Editor: Francesco Castellani

Received: 22 March 2024
Revised: 21 May 2024
Accepted: 23 May 2024
Published: 5 June 2024

Correction Statement: This article has been republished with a minor change. The change does not affect the scientific content of the article and further details are available within the backmatter of the website version of this article.

1. Introduction

Surface icing is crucial in various technical applications, particularly when surfaces are exposed/subjected to humid and cold air conditions [1–4]. Depending on the type of application and the accompanied risks, different strategies have been developed to address the problem of icing. Modern commercial airplanes have ice protection systems (IPS) that allow an all-weather flying capability. Nevertheless, active measures like thermal, electro-magnetic or pneumatic deicing systems require a lot of energy and are therefore restricted to cyclic operation [5,6]. In general aviation, the TKS-System (Tecalemit-Kilfrost-Sheepbridge Stokes) can prevent icing by pumping a fluid mixture through holes in the leading edge, creating a thin film. Like the fluid, which is used to deice commercial aircraft on the ground, it consists mainly of glycol alcohol [7]. Even though glycol ethers are not found to be persistent in the environment, not bio-accumulative and non-toxic, extensive use (e.g., on an airport in winter) could lead to problematic local concentrations [8,9]. In most cases, anti-icing and deicing chemicals contain 10–20% additives, including corrosion and rust inhibitors, thickening agents and surfactants which have a significant chronic toxicity [10]. Furthermore, the use of such chemicals is an additional cost factor for the industry.

Regarding wind power plants, icing of wind turbine rotor blades leads to a reduction in lift force and an increased drag force which causes a loss of production efficiency of up to 30% due to disturbed aerodynamics [11,12]. Furthermore, ice accumulation represents an increased health and safety risk due to ice shedding and ice throw in the turbines' vicinity [13,14]. Experiments conducted on a 300 kW wind turbine demonstrated that icing rates of >80 mm/h are possible and that the ice thickness increases towards the blade tip [15]. As countermeasures, thermal IPS are currently used almost exclusively, which are based on the heating of relevant rotor blade zones by electrically operated heating elements or a warm airflow circulating in the blade. The power requirement of electrical systems is 6–12% of the wind turbine output [16], and that of systems working with warm airflow is 10–15% [17]. In weather conditions that are particularly negative for operation, the power losses can also increase further to 80% [18] until it comes to the technically necessary shutdown [19]. Besides the efficiency loss, active heating of the rotor blades has to be monitored to not weaken the composite material over time [6].

Both aviation and wind energy would profit from passive icephobic surfaces, which reduce or delay ice accumulation and stimulate deicing by modification of surface topography and chemistry. Special coatings can be used as passive IPS, which are based on a reduction of the surface energy to achieve superhydrophobic and icephobic behavior [20]. Most polymer coatings are prone to erosion, which limits service life and thus prevents industrial use [6,21]. Metallic coatings show the potential to be erosion resistant but need further development to be strongly icephobic [22]. Laser structuring of surfaces is an alternative method to achieve superhydrophobic wetting behavior, triggered by creating air pockets in the solid/water interface and thereby forcing an incomplete wetting state (Cassie–Baxter), and/or through chemical modification of the material induced by the laser process itself [23]. Vercillo et al. [24] investigated the correlation between laser patterns, the resulting wettability and ice adhesion but used a chemical fluorinated solvent as a superhydrophobic and anti-ice coating. The results showed a direct correlation between the surface roughness and the ice adhesion, although all samples were superhydrophobic after dip coating. These findings are consistent with the results of our previous work, where shallow laser induced periodic surface structures (LIPSS) led to the lowest mechanical locking of the ice at the interface [25].

Under ambient air conditions, femtosecond laser processing induces a chemical reaction due to the laser's energy deposition [25,26]. This leads to a material-dependent oxidation process of the top surface layer, which adsorbs organic hydrocarbons from the air and thereby changes the overall chemical polarity from polar (hydrophilic) to non-polar (hydrophobic) [27]. This process is strongly dependent on the storage conditions (e.g., the chemical composition of the sample surrounding air) and can take from days to months [28]. Ways to shorten the wetting transformation time include heating [29] and vacuum treatment [30]. Our previous work presented a novel approach to significantly shorten the wetting transformation time by a hydrocarbon chemical treatment and compared it to vacuum treatment [31]. The best results were achieved by storing the laser-processed samples immersed in petrol. Depending on the laser-generated micro- or nano-structure, the ice adhesion could be reduced by 50% with petrol immersion and by 70% with vacuum treatment.

Nevertheless, it has to be considered that surface structures increase the roughness and could thereby alter the aerodynamics of a lift-generating body. The surface roughness is often characterized by the sand-grain roughness k, corresponding to the height of spherical particles attached to a surface like on a sandpaper [32]. Since real rough surfaces are more complex, the equivalent sand-grain roughness k_S can be estimated using different approaches. One widely used method for calculating k_S was developed by Flack et al. for $s_k > 0$ [33]:

$$k_S \approx 4.43 \cdot k_{RMS} \cdot (1 + s_k)^{1.37} \tag{1}$$

and for $s_k < 0$ [34]:

$$k_S \approx 2.73 \cdot k_{RMS} \cdot (2 + s_k)^{-0.45} \tag{2}$$

where k_{RMS} is the root-mean-square roughness height, and s_k is the skewness. A positive skewness indicates that the height distribution of the roughness is shifted below the mean plane (e.g., a turned surface), while a negative skewness indicates a shift above the mean plane (e.g., a pitted bearing surface) [35].

To quantify the effect of a rough surface on aerodynamics, Prikhod'ko et al. [36] tested a standard NACA 0012 airfoil with a modified rough surface (k_S = 200 μm) and measured a 7% decrease in maximum lift force and a twofold increase in drag when compared to a conventional smooth surface. Jung et al. [37] investigated the effect of wind turbine rotor blade roughness on its aerodynamic performance by simulating different wind speed scenarios. They applied an equivalent sand grain roughness height chord ratio k_S/c of 1.9×10^{-3}, where c is the chord length of the airfoil, to an S809 airfoil, which resulted in a performance decrease at 7 m/s but an increase at 10 m/s with a minor effect at higher wind speeds, which contradicts previous findings by Bouhelal et al. [38]. Based on 3D computational fluid dynamics (CFD) simulations, Bouhelal et al. concluded that roughness heights $k_s > 0.5$ μm decreased the performance by up to 35% at wind speeds > 10 m/s, but also found a wind speed dependence of the critical roughness value. It is commonly assumed that structured surfaces increase the friction and heat flux on the surface of an airfoil, thereby promoting ice growth which causes a further increase in surface roughness. Tagawa et al. [39] performed CFD airflow simulations for NACA 0012 airfoils considering the surface roughness due to ice accretion. The results showed that roughness effects become significant for equivalent sand-grain roughness heights $k_S/c > 1 \times 10^{-4}$, rapidly decreasing the maximum lift coefficient [39]. Prikhod'ko et al. [36] performed experiments with different leading edge shapes to simulate ice accretion and found that the formation of horn-like ice outgrowths causes a severe deterioration in the aerodynamic characteristics of the wing and thereby decreases the maximum lift force (down to 50%) and increases aerodynamic drag (by several times).

Besides the performance, a high erosion resistance is another critical property for future industrial applications of superhydrophobic and icephobic surfaces. In wind energy, contamination and erosion of blades (coatings) reduces the annual energy output of a turbine by 2–3.7% [40]. Sand, water and hail impacting the blades at high velocities cause the formation of pits, removal of coating and delamination of the underlying fiber-reinforced material. Most commercial anti-ice surfaces comprise thin polymer films which are prone to erosion. To address this limitation, both the scientific community and industry are actively developing erosion-resistant superhydrophobic and icephobic surfaces [41].

In this work, we expand our previous investigations on femtosecond laser surface processing and look at the performance and durability of superhydrophobic and icephobic surface layers formed by hydrocarbon and vacuum treatment. This study compares treatments and the influence of the laser-generated structure type on the wettability and the anti-ice performance. The generated surfaces were tested in the laboratory and the field. Wind tunnel tests were carried out to investigate the impact of these measures on the ice-accumulation process. The durability of the structures was evaluated during a six-month test campaign, where samples were placed on the rotor blades of a small-scale wind turbine located at an exposed mountain ridge.

2. Materials and Methods

2.1. Material

Cold-rolled stainless steel (1.4301/AISI 304) (Fixmetall Brunn am Gebirge, Austria) was used as substrate material for all experiments. The substrates were not polished before laser processing to keep their initial roughness from the cold rolling process. The thickness was 0.05 mm for wind tunnel and field tests, where flexible sheets were needed to fit the airfoil shapes. Before undergoing laser processing, the substrates were cleaned with acetone and air-dried.

2.2. Laser Processing

The samples were structured using a femtosecond laser system Femtopower Compact Pro (Spectra-Physics, Vienna, Austria) consisting of a Ti:Sapphire oscillator and a multi-pass Ti:Sapphire amplifier, which emits broadband 30 fs laser pulses at a rate of 1 kHz (Figure 1). Laser pulses can carry a maximum pulse energy of 0.8 mJ at 800 nm central wavelength and a bandwidth of 40 nm. Due to its internal setup, the output radiation is linearly polarized, which is required to form channel-like LIPSS. A variable attenuator was used to adjust the laser fluence on the specimens' surface. The laser beam was focused by a plano-convex spherical lens with a focal length of 100 mm. During all experiments, we worked with a Gaussian intensity distribution. Based on our previous experiments, we selected the same four different laser structure types for further testing (Figure 2). LIPSS were generated off-focus by overlapping linear tracks, grid and triangle structures were created by intersecting tracks at 90° or 60°, respectively. Micro dimple arrays were generated by repetitive static laser ablation.

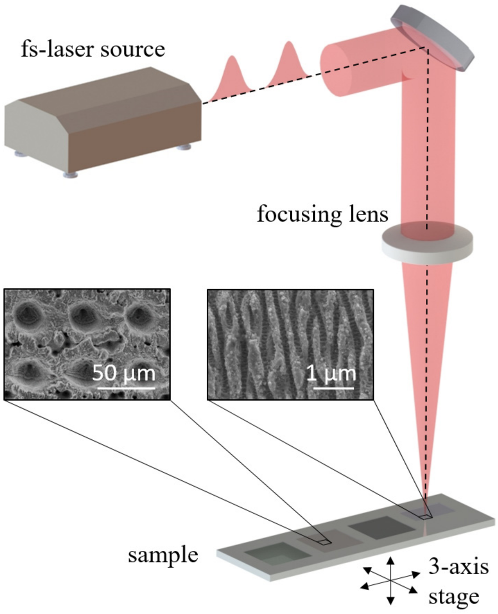

Figure 1. Schematic depiction of the femtosecond laser machining setup.

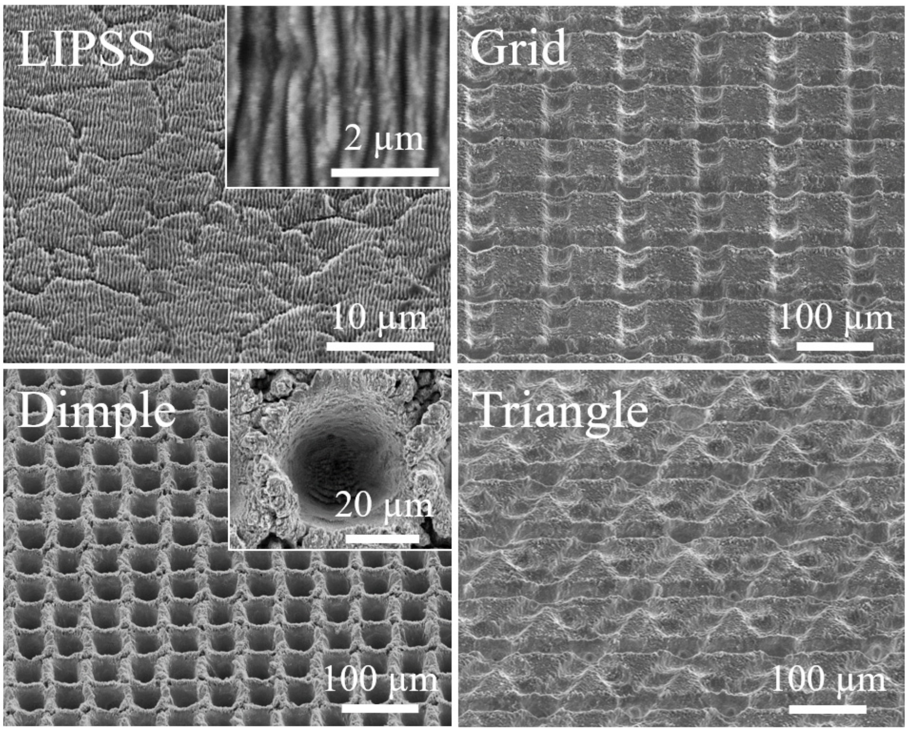

Figure 2. SEM images: laser-generated structure types, taken at a 45° tilt angle (close-ups were taken without tilt).

Samples were irradiated perpendicular to the surface (angle of incidence 0°) in a controlled environment at 21 °C ± 0.5 °C and a humidity of 45 ± 5% in air without the use of inert shielding gas. With the constant pulse repetition rate of 1 kHz, the number of laser pulses applied on the same surface area was adjusted by the feed rate of the 3-axis motorized translation stage. The machining parameters are summarized in Table 1.

Table 1. Laser machining parameters and post-laser-treatments of the samples which were tested in the icing wind tunnel (IWT—Icing Wind Tunnel; E—Erosion).

Sample ID	Structure Type	Wettability Treatment	Treatment Duration (h)	Laser Fluence (J/cm^2)	Spot Diameter (µm)	Hatch (µm)	Number of Laser Pulses
IWT#1	LIPSS	Vacuum	4	0.6	200	150	25
IWT#2	Grid	Vacuum	4	15	50	100	25
IWT#3	Dimple	Vacuum	4	20	50	50	40
IWT#4	Triangle	Vacuum	4	10	50	100	25
IWT#5	LIPSS	Petrol, immersion	4	0.6	200	150	25
IWT#6	Grid	Petrol, immersion	4	15	50	100	25
IWT#7	Dimple	Petrol, immersion	4	20	50	50	40
IWT#8	Triangle	Petrol, immersion	4	10	50	100	25
E#1	LIPSS	-	-	0.6	200	150	25
E#2	Grid	-	-	15	50	100	25
E#3	Dimple	-	-	20	50	50	20

2.3. Surface Structures

The geometric surface properties of the laser-processed samples were obtained with a Bruker Alicona Infinite Focus 3D surface measurement system, which uses the method of focus variation to retrieve surface topography information. For scanning electron microscopy (SEM) imaging, a JCM-5000 instrument (Jeol, Akishima, Japan) was used. Figure 2 shows the four structure types tested in the following experiments.

2.4. Wettability Acceleration Treatment

A contact angle goniometer OCA25 (DataPhysics, Filderstadt, Germany) with a 0.4 mm blunt tip cannula was used to evaluate the wettability properties of the laser treated samples. We used the sessile drop method with a polynomial fitting to obtain the static contact angles (SCA) utilizing a water drop volume of 10 µL.

Immediately after femtosecond laser processing, metal surfaces tend to be superhydrophilic and evolve to a hydrophobic state over a period of several days to weeks. To accelerate the wetting transformation time, the samples were placed in either a vacuum chamber or immersed in EuroSuper Petrol (RON 95) (OMV, Vienna, Austria) inside a sealed HDPE barrel (Table 1). We used the same SEM instrument (Jeol JCM-5000) for imaging and vacuum treatment, but we turned off the electron beam during the latter. Its turbomolecular pump provided a pressure of less than 10^{-4} mbar in the specimen chamber. The duration of the treatment was chosen based on our previous work, where the focus was on the wetting transformation time of laser-structured samples stored in different media. For this reason, the samples were treated for 2 weeks (336 h), even though, vacuum and petrol treatment showed a faster transformation. However, considering that only short transformation times are relevant for industrial applications, we reduced the treatment duration to 4 h in this work. The field tests were primarily focused on examining the mechanical erosion of the laser-generated structures in harsh environmental conditions, so no wettability treatment was applied.

2.5. Icing Wind Tunnel

The performance of the laser-processed and hydrocarbon/vacuum-treated samples under dynamic icing conditions was tested in the FH JOANNEUM small-scale icing wind tunnel (FHJIWT) (FH JOANNEUM, Graz, Austria) [42]. The FHJIWT is a calibrated closed-loop atmospheric wind tunnel of Göttingen configuration and can simulate in-flight icing conditions. For the experiments, laser-processed stainless steel foils were taped onto NACA 0012 airfoil segments (downscaled to 20%) with a nominal chord length of c = 200 mm made of extruded polystyrene (XPS) covered with a ply of fiberglass (Figure 3). As the investigation was focused on the icing of the leading edge, the air foil sections were truncated. The influence of possible vibrations caused by a turbulent wake of the blunt tip trailing edge was assumed to be neglectable based on the low wind speed and neutral angle of attack [43,44].

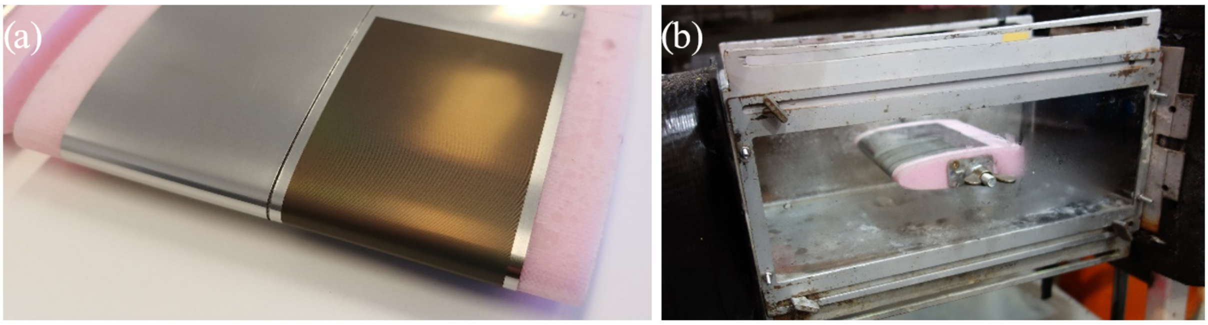

Figure 3. Airfoil section: (**a**) prepared sample IWT#1 with taped laser processed (**right**) and reference steel foil (**left**), (**b**) test section in the FHJIWT.

The 1.4301 metal sheets had a length of 150 mm and a width of 50 mm of which 120 × 45 mm were structured by the femtosecond laser with the machining parameters summarized in Table 1. Each sample consisted of one laser processed stainless steel foil placed side by side with an untreated reference foil (Figure 3). No spanwise or chordwise parting strip was used during the experiments. The icing tests were conducted in a representative glaze ice condition with a neutral angle of attack, AoA = 0° (Table 2).

Table 2. Icing conditions used in the wind tunnel experiments.

Ice Type	Temperature (°C)	Air Speed (m/s)	MVD * (µm)	LWC ** (gm^{-3}) @ −10 °C, 15 m/s	Icing Cycle (s)
Glaze	−10	25	42	5.1	180

* MVD—median volume diameter. ** LWC—liquid water content.

The initial wetting and ice growth were monitored and recorded by a camera for 180 s, positioned vertically on top of the test section. This view from above allowed us to assess both the initial wetting process as well as the ability of the surfaces to repel impinging water droplets and support runback along the upper airfoil surface. Prior to each run, the airfoils were mounted in the test section and acclimatized for 10 min.

To obtain more information on the ice accumulation after 180 s, the airfoil sections were removed from the test chamber and scanned with a portable 3D laser measurement system consisting of a Hexagon Absolute Arm and a RS6 laser-scanning head with a system accuracy of 48 µm. Therefore, a thin film of titanium-dioxide powder was applied to the accumulated ice to enhance the reflection of the laser light on the ice shape.

2.6. Field Tests

The erosion resistance of the laser-generated structures was tested using a small-scale wind turbine stationed on the Pretul mountain ridge in the Austrian Alps at an elevation of 1600 m. The wind turbine (superwind 1250) (superwind, Brühl, Germany) had a diameter of 2.4 m and a maximum wingtip speed of 75 m/s at 600 rpm. On each of the three wings, a small laser-structured stainless steel foil (1.4301) with a thickness of 50 µm was attached with an adhesive (Figure 4).

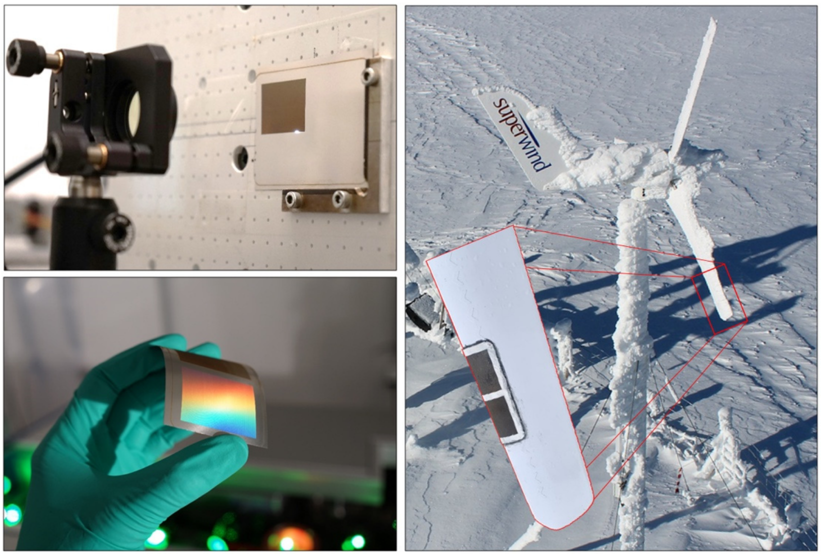

Figure 4. Femtosecond laser structuring process (**top left**), structured metal foil (**bottom left**); dynamic erosion field test setup with laser-structured stainless steel foils attached to rotor blades of a small-scale wind turbine (**right**).

The samples were prepared with laser machining parameters summarized in Table 1 (E#1–E#4). Environmental conditions were continuously measured and recorded over the experimental period of 6 months using an Eologix sensor (Figure 5). For further observation, a camera was installed to monitor the general state of the wind turbine (Figure 4). After the experiment, the wind turbine was dismantled and the relevant rotor blade sections were cut out for 3D surface characterization.

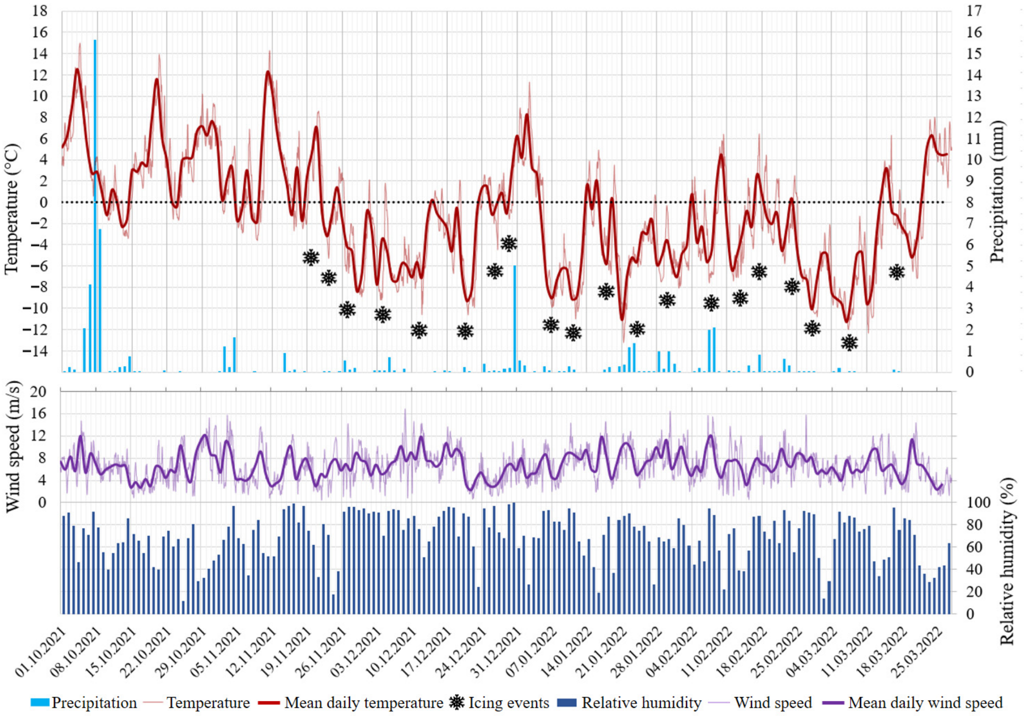

Figure 5. Environmental conditions during the dynamic erosion field test; Pretul mountain ridge at 1600 m elevation.

3. Results and Discussion

3.1. Icing Wind Tunnel

After the hydrocarbon/vacuum-treatment, all laser-structured flexible stainless steel samples showed superhydrophobic behavior (Table 3). By creating a rough surface, we tried to favor the Cassie–Baxter wetting mode, where vapor is "trapped" beneath the water fraction in the interface, over the Wenzel wetting mode, where the whole surface beneath the liquid is wetted, and thereby increase the hydrophobicity. Milne et al. [23] describe how the Cassie–Baxter equation is used to calculate the contact angle of a liquid on a rough surface and how to handle dual-scale rough surfaces, as produced by the laser ablation process. The icing wind tunnel performance (IWT performance) was evaluated visually by examining the wetting/icing videos taken during the experiment. Since the aerodynamic effect of the different laser structures applied to the surfaces could not be measured in this configuration, we focused our examination on the surfaces' ability to repel incoming water droplets and support runback. Furthermore, we visually evaluated the initial icing process, the resulting ice shape and the ice roughness on the leading edge.

Table 3. Wetting behavior of the stainless steel samples, before/after wind tunnel tests and anti-ice performance; delay time until ice beads occur on the leading edge; "+": more effective than reference surface; "~": similar to the reference surface; "−": less effective than reference sample.

Sample ID	**Structure Type**	**Wettability Treatment**	**SCA before IWT Tests (°)**	**SCA after IWT Tests (°)**	**IWT Performance**		
					Initial Water Runback	**Delay Time (s)**	**Ice Accumulation after 180 s**
IWT#1	LIPSS	Vacuum	151.3 ± 0.9	101.9 ± 16.8	~	0	−
IWT#2	Grid	Vacuum	157.0 ± 2.5	78.2 ± 6.3	~	0	−
IWT#3	Dimple	Vacuum	142.7 ± 4.7	61.9 ± 6.1	~	0	−
IWT#4	Triangle	Vacuum	158.7 ± 1.6	109.8 ± 7.9	~	0	−
IWT#5	LIPSS	Petrol immersion	131.9 ± 4.2	132.4 ± 14.3	+	0	−
IWT#6	Grid	Petrol immersion	148.5 ± 6.3	93.2 ± 2.3	+	50	−
IWT#7	Dimple	Petrol immersion	153.9 ± 2.3	84.0 ± 17.7	+	50	−
IWT#8	Triangle	Petrol immersion	144.2 ± 3.6	72.1 ± 20.2	+	50	−
Reference	-	-	94.2 ± 5.1	83.3 ± 12.6			

To highlight critical events like water runback after droplet impingement and the ice accretion phase, selected image sections of the recorded videos have been arranged, shown in Figure 6. The full videos are available as Supplementary Materials to this publication (Videos S1–S8).

Until the first ice layer formed on the surface, water was repelled more efficiently off the laser-structured and petrol-treated surfaces than vacuum-treated and reference surfaces. Samples IWT#6, IWT#7 and IWT#8 showed a smoother initial ice shape than the references (Figure 7). As the ice formation advanced, the growth of ice beads was initiated on the reference sections, starting at the airfoils upper surface and evolving towards the leading edge. In contrast, the leading edge sections of the structured samples remained smooth and showed less ice thickness.

Ice beads increase the leading edge roughness and induce a local laminar-turbulent flow transition [23]. Beads grow partially frozen and partially liquid until a certain height is reached, which depends on the air speed, AoA, LWC, MWD and temperature [45]. Subsequently, the liquid part runs back and fills the gaps between the following beads, and the excess liquid drains away as runback water. In the case of the petrol immersed samples IWT#6, IWT#7 and IWT#8, the formation of beads was delayed compared to the reference steel foil (Figure 7). During this delay, the surface remained smooth, which positively affected the aerodynamics of the airfoil. Experimental investigations performed with single UAV rotor blades in Appendix C icing conditions [46] have shown that, even a short icing encounter of one to two minutes can result in critical ice accretion [47]. A similar result was observed for a full-scale multirotor UAV in [48], where significant amounts of ice accreted on the rotor blades within minutes. The observed delay in ice bead formation shown in this study can extend the time a UAV has to leave the critical icing condition or land safely.

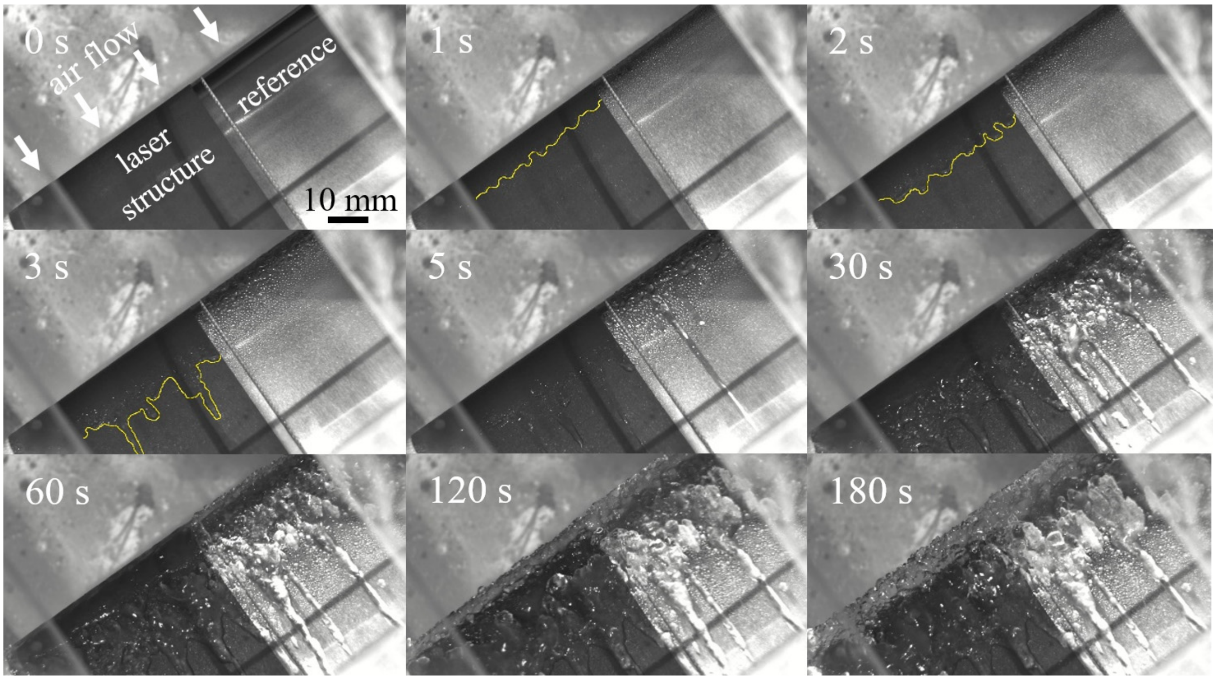

Figure 6. Top view of sample IWT#6—laser-generated grid structure with Eurosuper Petrol treatment (airfoil position: **left**), reference foil (airfoil position: **right**). Runback of arriving water droplets, waterfront highlighted by the yellow line (1–3 s), delayed ice bead buildup on the structured sample (30 s, 60 s).

For our calculations of the equivalent sand-grain roughness based on the method of Flack et al. [24,25] (Equations (1) and (2)), we decided to use the area root-mean-square height *Sq* instead of the line-based *Rq* and the same area equivalent *Ssk* for the skewness (Table 4).

Table 4. Measured roughness parameters of the samples tested in the IWT; equivalent sand-grain roughness k_S and chord length ratio k_S/c.

Structure Type	*Sq* (nm)	*Ssk*	k_S (µm)	k_S/c
LIPSS	82.2	0.18	0.46	2.28×10^{-6}
Grid	1816.4	−1.39	6.19	3.10×10^{-5}
Dimple	3190.6	0.07	15.51	7.75×10^{-5}
Triangle	2065.7	−1.28	6.54	3.27×10^{-5}

According to the results and conclusions of Prikhod'ko et al. [36], our laser-generated surface structures correspond to a smooth surface with an insignificant contribution to lift coefficient reduction, although the dimple structures showed a distinct micro-roughness. Based on that, no significant deterioration of aerodynamic performance was expected during our experiments since the highest equivalent sand-grain roughness that was tested resulted from dimple structures with k_S = 15.5 µm. Contrary to the findings of Prikhod'ko et al. [36], Bouhelal et al. [38] concluded that a roughness height above k_S = 0.5 µm leads to a deterioration of the aerodynamics of an airfoil at moderate wind speeds. Since there is a significant discrepancy between those results for the critical roughness heights, reaching from 0.5 µm to 200 µm, further work has to be carried out to evaluate the effect of the increased roughness of laser-structured surfaces on aerodynamics.

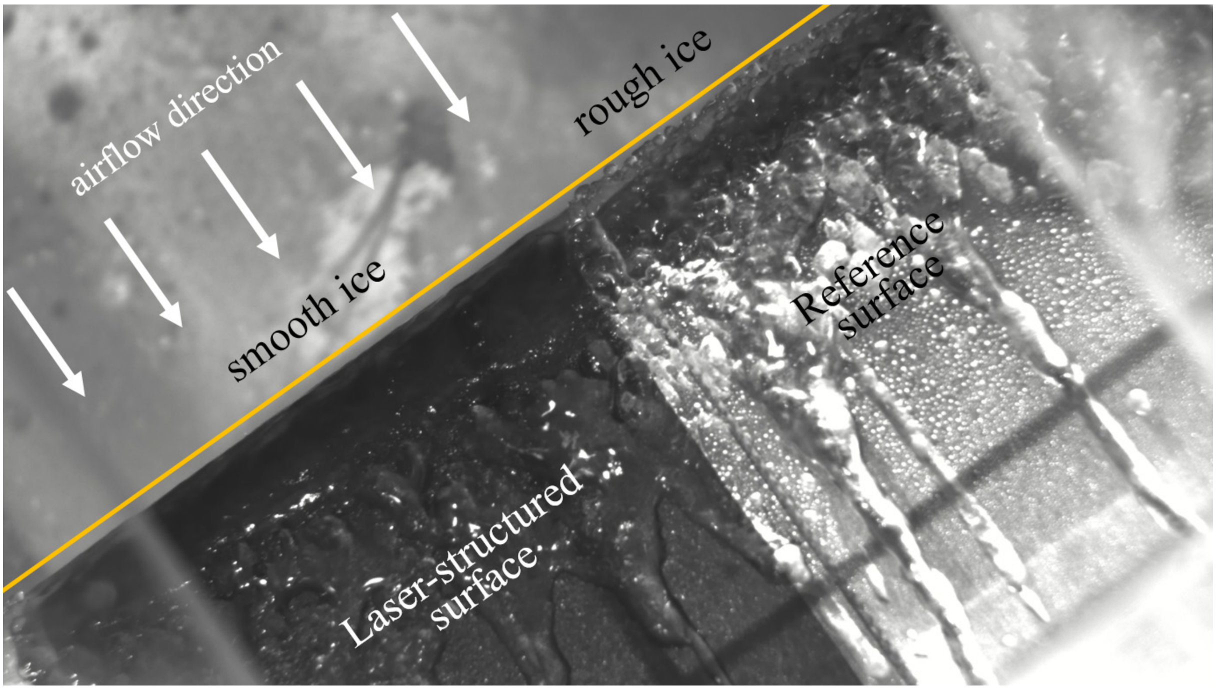

Figure 7. Top view of sample IWT#6 after 60 s, laser-structured sample (**left**) shows a smooth ice surface at the leading edge, while the same section on the reference surface (**right**) is already rough.

During the 180 s lasting icing cycle, a thick glaze ice layer built up on the leading edge, showing a horn-type ice shape (Figure 8). After the wind tunnel tests, the samples showed a significantly reduced SCA (Table 3). This phenomenon can be explained by the use of titanium-dioxide powder, which accumulated in the structures' roughness, thereby causing a transition from a Cassie–Baxter to a Wenzel wetting state. Attempts to remove the powder completely after the 3D ice scanning procedure failed. However, LIPSS nano-structures (IWT#1, IWT#5) were not affected similarly due to their shallow nature, resulting in a higher SCA.

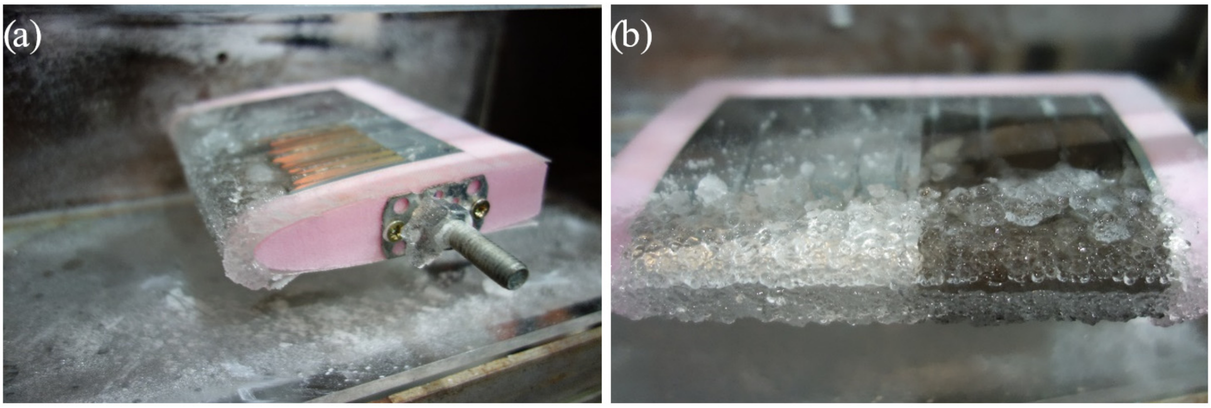

Figure 8. (**a**) Sample IWT#1 after 180 s of icing under glaze ice conditions, coloration of LIPSS due to diffraction; (**b**) Detail of the horn-like ice shape on the leading edge, laser-structured sample (**right**) and reference (**left**).

Example images of the 3D laser scans and the ice shapes in the leading edge area are shown in Figure 9. Unfortunately, it turned out that the icing time of 180 s was set too long, so the subsequent 3D ice measurement did not represent the delayed formation of ice beads on the laser-structured samples.

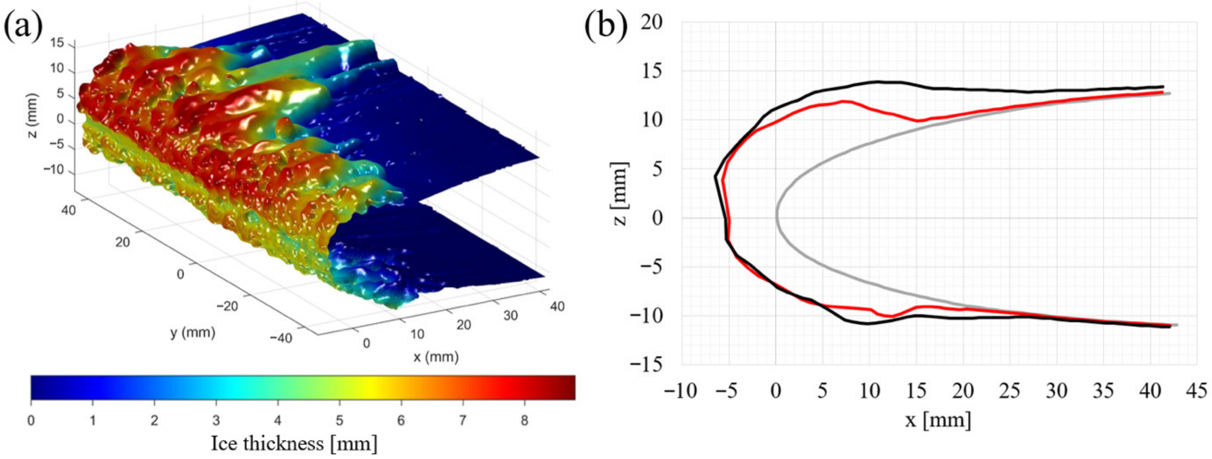

Figure 9. Result of a 3D laser scan of sample IWT#8 after 180 s in the icing wind tunnel; (**a**) ice accretion as a false color image—structured sample +y direction, reference –y direction; (**b**) averaged ice accumulation on the cross-section of the NACA 0012 airfoil (bold grey line); laser-structured surface (bold black line) shows increased ice accumulation compared to the reference sample (bold red line).

In contrast to the results of the video analysis, where samples IWT#6, IWT#7 and IWT#8 showed a smoother surface at the leading edge and a significantly delayed formation of ice beads, more ice volume accumulated on these surfaces after the entire test duration of 180 s. Since we did not use a chordwise parting strip between the structured and the reference surfaces, liquid water could have trickled from one side to the other, thereby influencing ice accumulation. Nevertheless, it could be shown that 4 h of Eurosuper petrol immersion could support the runback of impacting water droplets and positively influence the ice shape in the initial icing phase by effectively delaying the formation of beads (Table 3).

3.2. Erosion

A visual inspection of the samples, which had been attached to the rotor blades of a small-scale wind turbine for 6 months of field testing, revealed that they were physically still intact. The structural integrity of the steel foils remained unchanged, although the surface showed a slightly matte appearance. Due to the strong adhesive used to secure the samples on the rotor blades, the samples could not be removed without causing damage. Since the erosion of the blade has its maximum at the leading edge, the 3D topography characterization was therefore focused on these areas [49]. The surface topology was measured with 20 nm vertical and 1 µm lateral resolution. The spatial cut-off frequency λc was carefully selected to eliminate the leading edge curvature waveform while including the laser-generated structures in the resulting surface roughness (Table 5). Except for sample E#1, where LIPSS nano-structures were applied, all samples showed a reduction in surface roughness and also in the developed interfacial area ratio (*Sdr*), which describes the increase of surface area due to roughness and structures compared to the planar region. This reduction can be explained by erosion wear during 6 months of testing under cold climate conditions. Usually, the surface of wind turbine rotor blades is kept very smooth to reduce drag and extend the erosion incubation period. The only smooth surface in our experiment was sample E#1 with LIPSS applied. Due to the measurement system's limited lateral resolution, the surface characterization results of sample E#1 did not include the contribution of LIPSS. Further analysis of these structures via SEM and atomic force microscopy (AFM) revealed that LIPSS showed a mean spatial period of 560 nm and a vertical depth of 300 nm, consistent with previous findings for this laser/material combination [50].

Despite this limitation, the increase of *Sa*, *Sz* and *Sdr* indicates erosion wear of surface E#1. This was confirmed by a visual comparison of the unworn reference surface and the sample attached to the rotor blade (Figure 10). The 3D scan reveals macroscopic marks with a depth of about 1 µm on the surface of sample E#1 (Figure 10d,e). SEM analysis showed micrometer- and sub-micrometer-scale scratches and erosion of the LIPSS peaks, resulting in a smeared impression on the SEM images (Figure 10c,d).

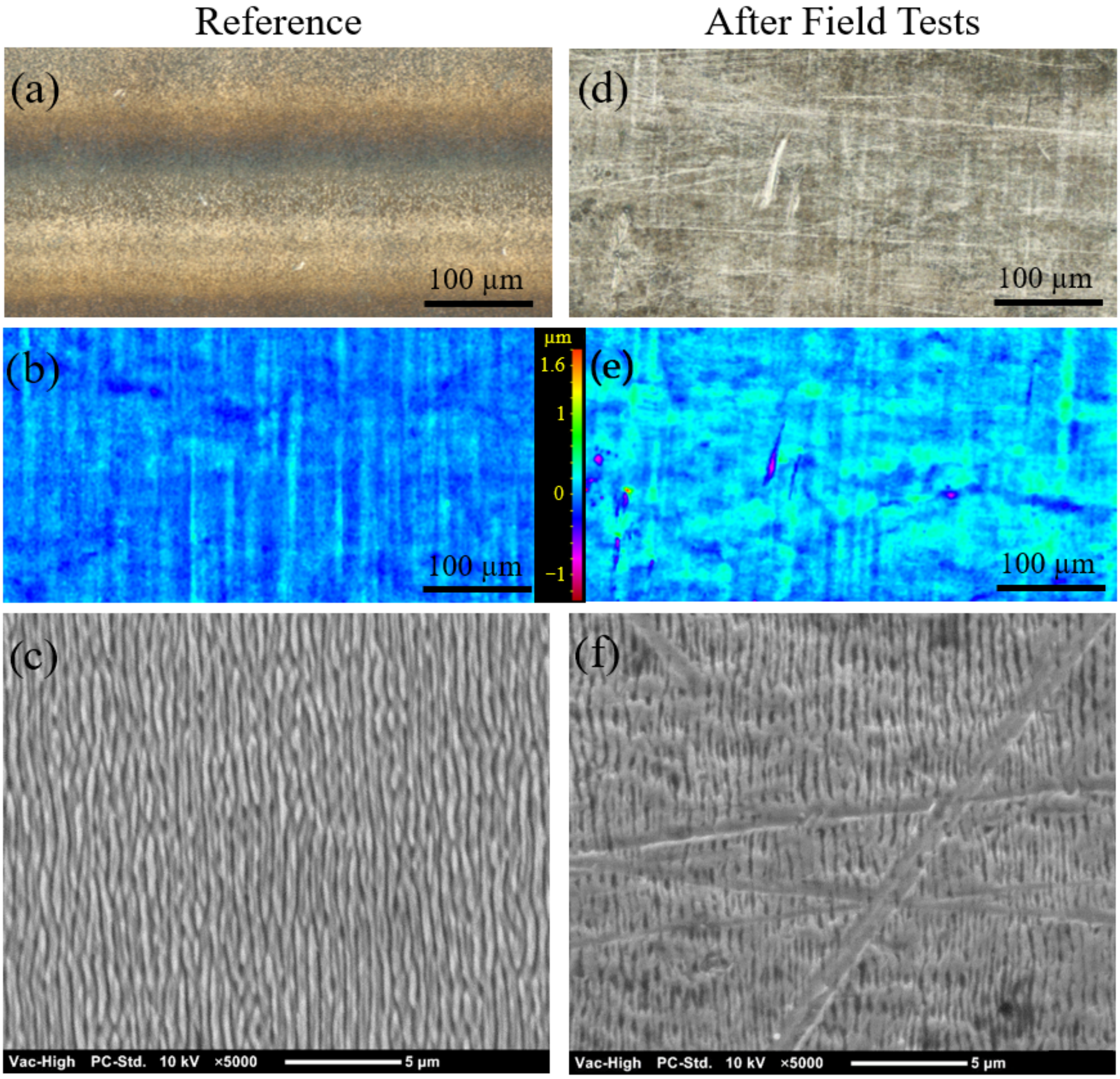

Figure 10. Three-dimensional scan of sample E#1 Reference (**left**) and sample E#1 after erosion test (**right**). Image of the measured field (**a**,**d**), 3D dataset in false colors (**b**,**e**) and SEM images of LIPSS nano-structures (**c**,**f**).

The visual inspection of the 3D surface topography of the larger structure types E#2, E#3 and E#4 revealed erosion wear consistent with the measured roughness (Figure 11, Table 5). The false color images indicated a reduction in the penetration depth of the roughness valleys, resulting from a shift of the mean roughness height towards the base material.

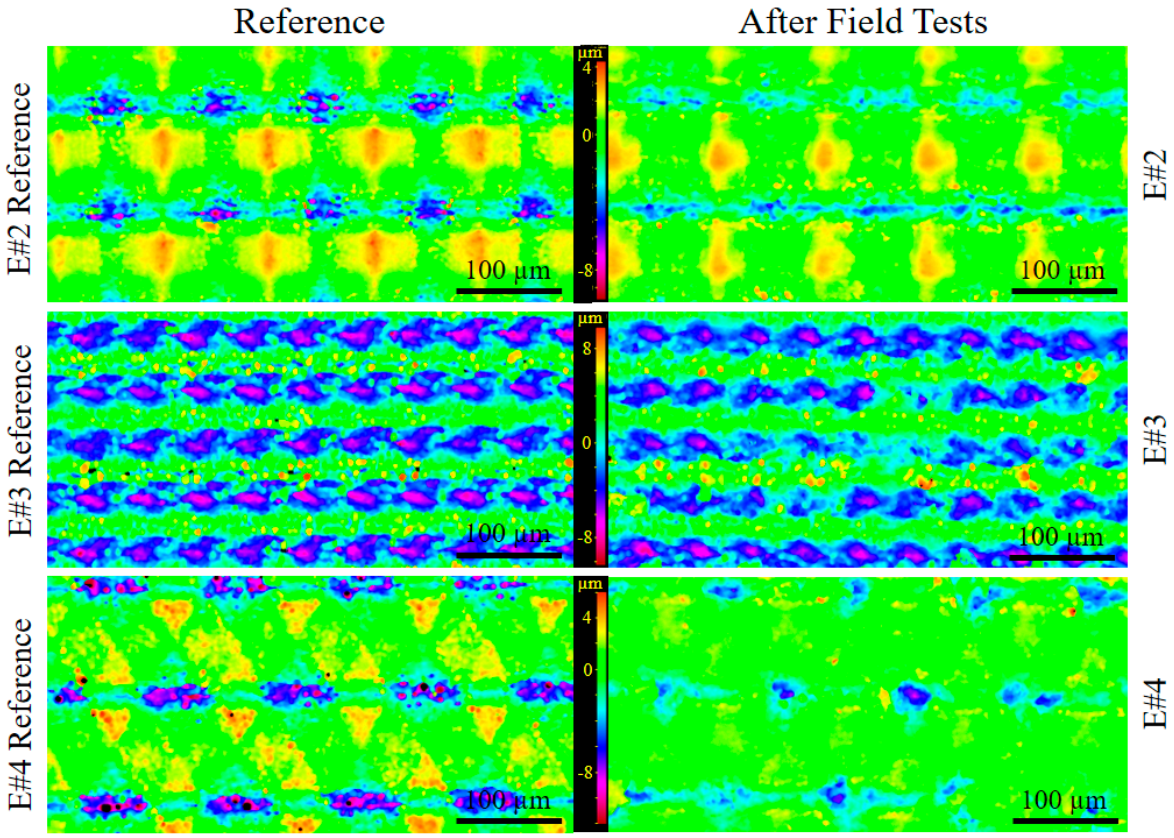

Figure 11. Three-dimensional scan of sample E#2 (grid), E#3 (dimple) and E#4 (triangle); reference samples (**left**) and eroded samples (**right**).

To improve laser-structured steel foils for erosion shield applications, other materials than 1.4301 could be investigated. Lee et al. [51], for example, performed droplet impact tests on various steels and demonstrated that erosion rates are coupled to the carbon content of the steel alloy and the surface hardness, where an increase in carbon and hardness leads to a decrease in erosion rate. According to DIN EN 10088-3:2022 the chemical composition of the used 1.4301 steel features a carbon content of 0.07 wt%, we measured a Vickers hardness of 182 HV. Following the correlation by Lee et al. [51], one could increase the lifetime of the laser-structured steel sheets by changing the composition to, e.g., 1.4305, which features a higher carbon content of 0.1 wt% and a ~10% higher hardness.

Table 5. Surface topography after laser processing and after field testing; *Sa*—arithmetic mean deviation; *Sq*—root mean square height; *Sz*—maximum height; *Sdr*—developed interfacial area ratio; *Sk*—core height.

Sample ID	Structure Type	Cut-off, λc (nm)	*Sa* (nm)	*Sq* (nm)	*Sz* (µm)	*Sdr* (%)	*Sk* (µm)
E#1 Reference	LIPSS	75	64.4	82.2	0.90	0.08	0.21
E#1	LIPSS	75	109.8	138.0	2.24	0.14	0.30
±			70.5%	68.0%	149.0%	61.4%	45.6%
E#2 Reference	Grid	150	1362.9	1816.4	14.32	25.00	3.55
E#2	Grid	150	1049.8	1301.2	9.93	7.66	3.08
±			−23.0%	−28.4%	−30.7%	−69.3%	−13.2%

Table 5. *Cont.*

Sample ID	Structure Type	Cut-off, λc (nm)	*Sa* (nm)	*Sq* (nm)	*Sz* (µm)	*Sdr* (%)	*Sk* (µm)
E#3 Reference	Dimple	300	2670.8	3190.6	19.26	136.53	9.66
E#3	Dimple	300	2448.9	2933.4	22.68	66.25	8.28
±			−8.3%	−8.1%	17.8%	−51.5%	−14.4%
E#4 Reference	Triangle	150	1604.4	2065.7	16.00	30.42	4.22
E#4	Triangle	150	1304.0	1685.7	18.95	19.51	3.06
±			−18.7%	−18.4%	18.4%	−35.9%	−27.5%

4. Conclusions

This paper studies the performance and durability of femtosecond laser-structured stainless steel of different topography. The focus was on the effect of the superhydrophobicity on the anti-ice properties under dynamic icing conditions (icing wind tunnel) and the erosion resistance of nano- and micro-structures in a long-term field test. To accelerate the wetting transformation time, improve hydrophobicity and reduce the ice adhesion, surfaces were stored in a vacuum and hydrocarbon liquid (Eurosuper petrol). The main conclusions are as follows:

- Femtosecond-laser-structured and petrol-treated stainless steel surfaces support the runback of impinging water droplets on an airfoil under glaze ice conditions.
- During the initial ice accretion, the petrol-treated samples showed a time delay of 50 s in ice bead build-up on the leading edge compared to the untreated reference surface. The accumulated ice was of a smoother shape, which should lead to improved aerodynamics during that phase.
- Long-term field tests demonstrated a high wear resistance of laser-generated structures on stainless steel, making them interesting for erosion shields in aviation and wind energy.

The measured delay in ice bead build-up could be very beneficial for, e.g., unmanned aerial vehicles (UAVs) which are very sensitive to icing and increase safety margins. Nevertheless, the wind tunnel tests showed an increased ice accumulation compared to the unstructured reference sample after a test duration of 180 s. Furthermore, it turned out that using titanium dioxide powder as a reflection enhancer for the laser assisted ice shape measurements did deteriorate the microstructures. Further experiments with shorter icing durations are needed to determine the effect of the icing delay and the initial smoother ice surface at the leading edge on the aerodynamics of the wing (drag and lift force measurements, simulations). After the erosion field test, the micro-structures showed slight erosion, resulting in a decreased surface roughness. Wear marks such as scratches of different sizes and depths were found on the LIPSS sample, which led to an increase in surface roughness—the nano-structures were largely preserved. For better erosion resistance, steel with a higher hardness than 1.4301, like 1.4305 could be used. Another approach would be the application of thin layers of erosion resistant material such as metal- or ceramic-nitride compounds, although this impacts surface energy and hence wetting.

Supplementary Materials: The following supporting information can be downloaded at: https://www.mdpi.com/article/10.3390/wind4020008/s1, Video S1: IWT#1; Video S2: IWT#2; Video S3: IWT#3; Video S4: IWT#4; Video S5: IWT#5; Video S6: IWT#6; Video S7: IWT#7; Video S8: IWT#8.

Author Contributions: Conceptualization, R.F. and G.L.; methodology, R.F.; software, R.F.; validation, R.F. and G.L.; formal analysis, R.F. and G.L.; investigation, R.F.; resources, G.L. and A.O.; data curation, R.F., G.G. and G.L.; writing—original draft preparation, R.F. and G.G.; writing—review and editing, R.F., G.L. and A.O.; visualization, R.F.; supervision, G.L. and A.O.; project administration, G.L. and R.F.; funding acquisition, G.L., R.F. and A.O. All authors have read and agreed to the published version of the manuscript.

Funding: This research has received funding from the Austrian Research Promotion Agency FFG "Take Off" program, project number 43317863 and the Austrian Climate and Energy Fund with FFG project number 871733.

Institutional Review Board Statement: Not applicable.

Informed Consent Statement: Not applicable.

Data Availability Statement: The original contributions presented in the study are included in the article/Supplementary Material, further inquiries can be directed to the corresponding author.

Acknowledgments: The authors acknowledge the FH Joanneum as well as the Austrian Institute for Icing Sciences for their support during the icing wind tunnel tests and the Energiewerkstatt for their contribution to the field tests. The authors also thank the University Service Centre for Transmission Electron Microscopy (USTEM) at TU Wien for their support on scanning electron microscopy. The authors acknowledge Open Access Funding by TU Wien.

Conflicts of Interest: The authors declare no conflicts of interest.

References

1. Muhammed, M.; Virk, M.S. Ice accretion on rotary-wing unmanned aerial vehicles—A review study. *Aerospace* **2023**, *10*, 261. [CrossRef]
2. Kang, W.; Xue, Y.; Tian, H.; Wang, M.; Wang, X. The impact of icing on the airfoil on the lift-drag characteristics and maneuverability characteristics. *Math. Probl. Eng.* **2021**, *2021*, 5568740. [CrossRef]
3. Goshima, N.; Maeda, T.; Kamada, Y.; Tada, T.; Hanamura, M.; Pham, H.H.; Iwai, K.; Fujiwara, A.; Hosomi, M. Study on influence of blade icing on operational characteristics of wind turbine at cold climate. *J. Phys. Conf. Ser.* **2020**, *1618*, 052021. [CrossRef]
4. Abdelaal, A.; Nims, D.; Jones, K.; Sojoudi, H. Prediction of ice accumulation on bridge cables during freezing rain: A theoretical modeling and experimental study. *Cold Reg. Sci. Technol.* **2019**, *164*, 102782. [CrossRef]
5. Karpen, N.; Diebald, S.; Dezitter, F.; Bonaccurso, E. Propeller-integrated airfoil heater system for small multirotor drones in icing environments: Anti-icing feasibility study. *Cold Reg. Sci. Technol.* **2022**, *201*, 103616. [CrossRef]
6. Parent, O.; Ilinca, A. Anti-icing and de-icing techniques for wind turbines: Critical review. *Cold Reg. Sci. Technol.* **2011**, *65*, 88–96. [CrossRef]
7. Goraj, Z. An overview of the deicing and antiicing technologies with respects for the future. In Proceedings of the 24th International Congress of the Aeronautical Sciences, Yokohama, Japan, 29 August–3 September 2004.
8. Staples, C.A.; Boatman, R.J.; Cano, M.L. Ethylene glycol ethers: An environmental risk assessment. *Chemosphere* **1998**, *36*, 1585–1613. [CrossRef]
9. Hu, H.; Liu, Y.; Gao, L. *Wind Turbine Icing Physics and Anti-/De-Icing Technology*; Elsevier: Amsterdam, The Netherlands, 2022; ISBN 978-0-12-824532-3.
10. Ramakrishna, D.M.; Viraraghavan, T. Environmental impact of chemical deicers—A Review. *Water Air Soil Pollut.* **2005**, *166*, 49–63. [CrossRef]
11. Hochart, C.; Fortin, G.; Perron, J.; Ilinca, A. Wind turbine performance under icing conditions. *Wind Energy* **2008**, *11*, 319–333. [CrossRef]
12. Homola, M.C.; Virk, M.S.; Nicklasson, P.J.; Sundsbø, P.A. Performance losses due to ice accretion for a 5 MW wind turbine. *Wind Energy* **2011**, *15*, 379–389.
13. Seifert, H.; Wsterhellweg, A.; Kröning, J. Risk analysis of ice throw from wind turbines. *Boreas* **2003**, *6*, 2006-01.
14. Morgan, C.; Bossanyi, E.; Seifert, M.H. Assessment of safety risks arising from wind turbine icing. *Boreas* **1998**, *4*, 113–121.
15. Shu, L.; Li, H.; Hu, Q.; Jiang, X.; Qiu, G.; McClure, G.; Yang, H. Study of ice accretion feature and power characteristics of wind turbines at natural icing environment. *Cold Reg. Sci. Technol.* **2018**, *147*, 45–54. [CrossRef]
16. Laakso, T.; Baring-Gould, I.; Durstewitz, M.; Horbaty, R.; Lacroix, A.; Peltola, E.; Ronsten, G.; Tallhaug, L.; Wallenius, T. *State-of-the-Art of Wind Energy in Cold Climates*; VTT: Espoo, Finland, 2010; Volume 152. (In English)
17. Battisti, L.; Fedrizzi, R.; Brighenti, A.; Laakso, T. Sea ice and icing risk for offshore wind turbines. In Proceedings of the OWEMES, Citavecchia, Italy, 20–22 April 2006; pp. 20–22.
18. Gao, L.; Tao, T.; Yongqian, L.; Hui, H. A field study of ice accretion and its effects on the power production of utility-scale wind turbines. *Renew. Energy* **2021**, *167*, 917–928. [CrossRef]
19. Kjersem, H.A. Estimation of Production Losses Due to Icing on Wind Turbines at Kvitfjell Wind Farm. Master Thesis, Norwegian University of Life Sciences, Ås, Norway, 2019.
20. Huang, X.; Tepylo, N.; Pommier-Budinger, V.; Budinger, M.; Bonaccurso, E.; Villedieu, P.; Bennani, L. A survey of icephobic coatings and their potential use in a hybrid coating/active ice protection system for aerospace applications. *Prog. Aerosp. Sci.* **2019**, *105*, 74–97. [CrossRef]
21. Slot, H.M.; Gelinck, E.R.M.; Rentrop, C.; van der Heide, E. Leading edge erosion of coated wind turbine blades: Review of coating life models. *Renew. Energy* **2015**, *80*, 837–848. [CrossRef]

22. Soltis, J.; Palacios, J.; Eden, T.; Wolfe, D. Evaluation of Ice-Adhesion Strength on Erosion-Resistant Materials. *AIAA J.* **2015**, *53*, 1825–1835. [CrossRef]
23. Milne, A.J.B.; Amirfazli, A. The Cassie equation: How it is meant to be used. *Adv. Colloid Interface Sci.* **2012**, *170*, 48–55. [CrossRef]
24. Vercillo, V.; Tonnicchia, S.; Romano, J.-M.; García-Girón, A.; Aguilar-Morales, A.I.; Alamri, S.; Dimov, S.S.; Kunze, T.; Lasagni, A.F.; Bonaccurso, E. Design rules for laser-treated icephobic metallic surfaces for aeronautic applications. *Adv. Funct. Mater.* **2020**, *30*, 1910268. [CrossRef]
25. Fürbacher, R.; Liedl, G. Investigations on the wetting and deicing behavior of laser treated hydrophobic steel surfaces. In Proceedings of the Laser-Based Micro-Nanoprocessing XV, Online, 6–12 March 2021. [CrossRef]
26. Yang, Z.; Liu, X.; Tian, Y. Insights into the wettability transition of nanosecond laser ablated surface under ambient air exposure. *Adv. Colloid Interface Sci.* **2019**, *533*, 268–277. [CrossRef]
27. Hauschwitz, P.; Jagdheesh, R.; Rostohar, D.; Brajer, J.; Kopeček, J.; Jiřícek, P.; Houdková, J.; Mocek, T. Hydrophilic to ultrahydrophobic transition of Al 7075 by affordable ns fiber laser and vacuum processing. *Appl. Surf. Sci.* **2020**, *505*, 144523. [CrossRef]
28. Cardoso, J.T.; Garcia-Girón, A.; Romano, J.M.; Huerta-Murillo, D.; Jagdheesh, R.; Walker, M.; Dimov, S.S.; Ocaña, J.L. Influence of ambient conditions on the evolution of wettability properties of an IR-, ns-laser textured aluminium alloy. *RSC Adv.* **2017**, *7*, 39617–39627. [CrossRef]
29. Ngo, C.-V.; Chun, D.-M. Fast wettability transition from hydrophilic to superhydrophobic laser-textured stainless steel surfaces under low-temperature annealing. *Appl. Surf. Sci.* **2017**, *409*, 232–240. [CrossRef]
30. Jagdheesh, R.; Diaz, M.; Marimuthu, S.; Ocana, J.L. Robust fabrication of µ-patterns with tunable and durable wetting properties: Hydrophilic to ultrahydrophobic via a vacuum process. *J. Mater. Chem.* **2017**, *5*, 7125–7136. [CrossRef]
31. Fürbacher, R.; Liedl, G.; Otto, A. Fast transition from hydrophilic to superhydrophobic, icephobic properties of stainless steel samples after femtosecond laser processing and exposure to hydrocarbons. *Procedia CIRP* **2022**, *111*, 643–647. [CrossRef]
32. Kadivar, M.; Tormey, D.; McGranaghan, G. A review on turbulent flow over rough surfaces: Fundamentals and theories. *Int. J. Thermofluids* **2021**, *10*, 100077. [CrossRef]
33. Flack, K.A.; Schultz, M.P. Review of hydraulic roughness scales in the fully rough regime. *J. Fluids Eng.* **2010**, *132*, 041203. [CrossRef]
34. Flack, K.A.; Schultz, M.P.; Barros, J.M. Skin friction measurements of systematically-varied roughness: Probing the role of roughness amplitude and skewness. *Flow Turbul. Combust.* **2019**, *104*, 317–329. [CrossRef]
35. Leach, R.K. Surface topography characterization. In *Fundamental Principles of Engineering Nanometrology*, 2nd ed.; William Andrew Publishing: Norwich, UK, 2014; pp. 211–262.
36. Prikhod'ko, A.A.; Alekseenko, S.V.; Chmovzh, V.V. Experimental investigation of the influence of the shape of ice outgrowths on the aerodynamic characteristics of the wing. *J. Eng. Phys. Thermophys.* **2019**, *92*, 486–492. [CrossRef]
37. Jung, Y.S.; Baeder, J. Simulations for effect of surface roughness on wind turbine aerodynamic performance. *J. Phys. Conf. Ser.* **2020**, *1452*, 012055. [CrossRef]
38. Bouhelal, A.; Smaïli, A.; Masson, C.; Guerri, O. Effects of surface roughness on aerodynamic performance of horizontal axis wind turbines. In Proceedings of the 25th Annual Conference of the Computational Fluid Dynamics Society of Canada, CFD2017-337, Windsor, ON, Canada, 18–21 June 2017.
39. Tagawa, G.B.S.; Morency, F.; Beaugendre, H. CFD investigation on the maximum lift coefficient degradation of rough airfoils. *AIMS Energy* **2021**, *9*, 305–325. [CrossRef]
40. Han, W.; Kim, J.; Kim, B. Study on correlation between wind turbine performance and ice accretion along a blade tip airfoil using CFD. *J. Renew. Sustain. Energy* **2018**, *10*, 023306. [CrossRef]
41. Zeng, D.; Li, Y.; Huan, D.; Liu, H.; Luo, H.; Cui, Y.; Zhu, C.; Wang, J. Robust epoxy-modified superhydrophobic coating for aircraft anti-icing systems. *Coll. Surf. A Phys. Eng. Asp.* **2021**, *628*, 127377. [CrossRef]
42. Puffing, R.F.A.; Peciar, M.; Hassler, W. Instrumentation of an icing wind tunnel based on SAE standards. *Sci. Proc. Fac. Mech. Eng. STU* **2013**, *21*, 37–43. [CrossRef]
43. Thomareis, N.; Papadakis, G. Effect of trailing edge shape on the separated flow characteristics around an airfoil at low Reynolds number: A numerical study. *Phys. Fluids* **2017**, *29*, 014101. [CrossRef]
44. Hu, J.; Wang, Z.; Zhao, W.; Sun, S.; Sun, C.; Guo, C. Numerical simulation on vortex shedding from a hydrofoil in steady flow. *J. Mar. Sci. Eng.* **2020**, *8*, 195. [CrossRef]
45. Fortin, G.; Ilinca, A.; Laforte, J.-L.; Brandi, V. New roughness computation method and geometric accretion model for airfoil icing. *J. Aircr.* **2004**, *41*, 119–127. [CrossRef]
46. Airworthiness standards: Transport category airplanes. In *Code of Federal Regulations, Title 14, Chapter I, Subchapter C, Part 25, Appendix C*, 1-1-23 ed.; Federal Aviation Administration: Washington, DC, USA, 2023.
47. Kozomara, D.; Amon, J.; Puffing, R.; Neubauer, T.; Schweighart, S.; Diebald, S.; Rapf, A.; Moser, R.; Breitfuss, W. Experimental investigation of UAS rotors and ice protection systems in appendix C icing conditions. In Proceedings of the International Conference on Icing of Aircraft, Engines, and Structures, Vienna, Austria, 20–23 June 2023; SAE Technical Paper Series. [CrossRef]
48. Kozomara, D.; Neubauer, T.; Puffing, R.; Bednar, I.; Breitfuss, W. Experimental investigation on the effects of icing on multicopter UAS operation. In Proceedings of the AIAA AVIATION, Virtual, 2–6 August 2021. [CrossRef]

49. Liersch, L.; Michael, J. Investigation of the impact of rain and particle erosion on rotor blade aerodynamics with an erosion test facility to enhancing the rotor blade performance and durability. *J. Phys. Conf. Ser.* **2014**, *524*, 012023. [CrossRef]
50. Fuerbacher, R.; Liedl, G.; Murzin, S.P. Experimental study of spatial frequency transition of laser induced periodic surface structures. *J. Phys. Conf. Ser.* **2021**, *1745*, 012017. [CrossRef]
51. Lee, G.M.C. The erosion resistance of plain carbon steels under water droplet impact conditions. *Wear* **1990**, *141*, 185–201. [CrossRef]